Microstructural and Optical Properties of MgAl₂O₄ Spinel: Effects of Mechanical Activation, Y₂O₃ and Graphene Additions

Nina Obradovic [1,*], William G. Fahrenholtz [2], Cole Corlett [2], Suzana Filipovic [1], Marko Nikolic [3], Bojan A. Marinkovic [4], Simone Failla [5], Diletta Sciti [5], Daniele Di Rosa [6] and Elisa Sani [6]

1   Institute of Technical Sciences, Serbian Academy of Sciences and Arts, 11000 Belgrade, Serbia; suzana.filipovic@itn.sanu.ac.rs
2   Materials Science and Engineering, Missouri University of Science and Technology, Rolla, MO 65409, USA; billf@mst.edu (W.G.F.); colecorlett10@gmail.com (C.C.)
3   Institute of Physics Belgrade, 11000 Belgrade, Serbia; nikolic@ipb.ac.rs
4   Departamento de Engenharia Química e de Materiais, Pontifícia Universidade Católica do Rio de Janeiro, Rio de Janeiro 22250-000, Brazil; bojan@puc-rio.br
5   Institute of Science and Technology for Ceramics (ISTEC), 48018 Faenza, Italy; simone.failla@istec.cnr.it (S.F.); diletta.sciti@istec.cnr.it (D.S.)
6   National Institute of Optics, National Research Council (CNR-INO), 50125 Firenze, Italy; daniele.dirosa@ino.it (D.D.R.); elisa.sani@ino.it (E.S.)
*   Correspondence: nina.obradovic@itn.sanu.ac.rs

Abstract: Magnesium aluminate and other alumina-based spinels attract attention due to their high hardness, high mechanical strength, and low dielectric constant. MgAl₂O₄ was produced by a solid-state reaction between MgO and α-Al₂O₃ powders. Mechanical activation for 30 min in a planetary ball mill was used to increase the reactivity of powders. Yttrium oxide and graphene were added to prevent abnormal grain growth during sintering. Samples were sintered by hot pressing under vacuum at 1450 °C. Phase composition and microstructure of sintered specimens were characterized by X-ray powder diffraction and scanning electron microscopy. Rietveld analysis revealed 100% pure spinel phase in all sintered specimens, and a decrease in crystallite size with the addition of yttria or graphene. Density measurements indicated that the mechanically activated specimen reached 99.6% relative density. Furthermore, the highest solar absorbance and highest spectral selectivity as a function of temperature were detected for the mechanically activated specimen with graphene addition. Mechanical activation is an efficient method to improve densification of MgAl₂O₄ prepared from mixed oxide powders, while additives improve microstructure and optical properties.

Keywords: mechanical activation; dopants; sintering; optical properties

1. Introduction

Magnesium aluminate spinel, MgAl₂O₄, the only compound in the MgO-Al₂O₃ binary system at ambient pressure, is a ceramic of great importance in modern technologies due to its high hardness, high melting point and low dielectric constant [1]. It is attractive also due to its corrosion resistance, mechanical properties, and low cost [2,3]. When fully dense, pure MgAl₂O₄ can be transparent in visible light. The properties of ceramics strongly depend on the composition, nature of powders, impurities or additives, and fabrication methods [4]. Many different routes have been used to synthesize dense spinel-based ceramics such as hot pressing, pressureless methods, spark plasma, and microwave sintering utilizing spinel powder as the raw material, with or without sintering additives [5–12]. Some authors have reported on direct solid-state reactions of oxides, wet chemical precipitation, and mechanical activation [13–19]. The choice of synthesis method is based on the desired particle size and purity of the spinel powder. Additionally, preparation conditions have a great impact on the final microstructure and properties of ceramic materials [20].

Hot pressing (HP) has been recognized as an advanced method for ceramic fabrication. HP is a fast and efficient sintering technique that uses applied pressure and low-strain-rate powder metallurgy process for forming of a powder or powder compact at a temperature high enough to induce sintering and creep processes [21]. HP can use high heating rates (50 °C·min^{-1} or higher) and short non-isothermal sintering times (30 min or less), and it is considered an excellent method for preparing nanostructured ceramics and nanocomposites [21,22]. Compared to conventional sintering processes, HP can significantly shorten the sintering time to few minutes and can promote full densification of materials which are difficult to sinter using conventional sintering techniques. The key issue in all sintering approaches is controlling the grain growth/densification behavior. One of the possible ways to prevent grain growth during sintering is addition of very small quantities of various compounds (Y_2O_3, LiF, NaF, AlN, etc.). Another alternative, prior to sintering, is mechanical activation (MA), which is a high-energy ball milling process that induces physicochemical changes in spinels [16–18,23–27]. MA produces defects in materials which increase the chemical activity and accelerate mechanisms of sintering. Increasing the speed of the process decreases the sintering time and temperature [28,29]. Furthermore, mechanical activation can also affect the final physical properties of sintered bodies [30]. Such milling processes are attractive methods, because they enable the formation of submicron and/or nanostructured materials with desirable properties [31].

In the present work, we report the influence of MA, in combination with additives, on densification and the final properties of $MgAl_2O_4$ sintered bodies. We focused on studying doped spinel (concentration of the Y_2O_3 0.1 wt.%, and graphene 1 wt.%) to improve their optical properties. X-ray powder diffraction (XRPD), scanning electron microscopy (SEM), and UV–visible spectroscopy were used for characterization of the as-prepared samples.

2. Experimental Methods

A mixture of high-purity MgO and α-Al_2O_3 starting powders (all 99.9% purity Sigma–Aldrich, p.a., St. Louis, MO, USA) was used in these experiments. The starting MgO and α-Al_2O_3 powders were added in a one-to-one molar ratio to produce stoichiometric $MgAl_2O_4$. The powders were mixed by ball milling for 1 min to homogenize them without significant particle size reduction. A portion of the as-obtained powders was additionally mechanically activated for 30 min in a high-energy planetary ball mill (Planetary Ball Mill Retsch PM 100, Haan, Germany) in air. One wt.% of graphene (99.9% purity Sigma–Aldrich, p.a., St. Louis, MO, USA) was added to a second powder mixture prior to activation, while another batch of powder contained 0.1 wt.% of Y_2O_3 (99.99% purity, Pangea International Ltd.-Shanghai, China). The first steps of homogenization and mechanical activation were performed using the same mill with Y-stabilized ZrO_2 vials and balls. The media were 5 mm in diameter. The ball-to-powder weight ratio was 40:1, with a rotation speed of 400 rpm. Powders were sieved after milling. The powder mixtures were labelled as HP1 (ball milled plus 30 min mechanical activation), HP2 (ball milled only), HP3 (30 min activated with yttrium addition), and HP4 (30 min activated with graphene addition). Powders were hot pressed in a graphite die (Ø = 30 mm) at 1450 °C in vacuum (20 Pa), with an applied pressure of 30 MPa, heating ramp 30 °C·min^{-1}, and free cooling and dwelling times were between 5–10 min (see Table 1).

Table 1. Starting composition, sintering parameters, densities.

Name	Composition	Process	Temperature	Pressure	Dwell Time at T_{MAX}	Height	Weight	Bulk Density
			°C	MPa	min	mm	g	g·cm^{-3}
HP1	Al_2O_3 + MgO	Planetary			5	7.5	19.35	3.52
HP2	Al_2O_3 + MgO	Ball milled only	1450	30	10	8.04	18.84	3.46
HP3	Al_2O_3 + MgO + 0.1 wt.% Y_2O_3	Planetary			5	7.1	18.55	3.55
HP4	Al_2O_3 + MgO + 1 wt.% C	Planetary			6	7.5	19.49	3.47

The procedure used for synthesis and densification of the spinel materials in the present study is based on our previous manuscript [13] and briefly summarized in the present paper. Densities of sintered specimens were calculated by Archimedes' principle. Sintered specimens were subjected to X-Ray powder diffraction (XRPD; X'Pert Pro, PANalytical, Almelo, Netherlands) in the Bragg–Brentano geometry using Cu-Kα radiation. Measurements were conducted on polished cross sections of the hot-pressed specimens. Phase analysis was performed by Rietveld refinement (RIQAS4, Materials Data Incorporated, Livermore, CA, USA). Lattice parameters determined using Rietveld refinement of XRD data were used to calculate the theoretical density of sintered bodies, assuming cubic crystal structure and the space group Fd$\bar{3}$m (227). Microstructure was examined by scanning electron microscopy (SEM; Raith eLine, Raith GmbH, Islandia, NY, USA). The samples were polished cross sections that were coated with a conductive Au/Pd coating before placing into the SEM.

Room-temperature hemispherical optical reflectance and transmittance spectra for quasinormal incidence angle have been acquired from polished cross sections using two instruments: a double-beam spectrophotometer (Perkin Elmer Lambda900, MA, USA) with a 150 mm-diameter Spectralon®-coated integration sphere for the 0.25–2.5 µm wavelength region, and a Fourier transform infrared spectrometer (FT-IR Bio-Rad Excalibur, CA, USA) with gold-coated integrating sphere and liquid nitrogen-cooled detector for the spectral range 2.5–15.7 µm. From experimental reflectance ($R^{\cap}(\lambda)$) and transmittance ($T^{\cap}(\lambda)$) data, the spectral absorbance $\alpha(\lambda)$ or emittance $\varepsilon(\lambda)$ can be obtained, as:

$$\alpha(\lambda) = 1 - R^{\cap}(\lambda) - T^{\cap}(\lambda) = \varepsilon(\lambda) \tag{1}$$

Thicknesses of samples are 6.50 mm for HP1, 6.90 mm for HP2 and HP3 and 6.95 mm for HP4.

3. Results and Discussion

Figure 1 shows the specimens after sintering. All specimens were disc shaped. The ones with graphene additions were black, and the rest were white or grey. They all achieved relative densities over 96%.

Figure 1. Sintered specimens: HP1—30 min-activated sample, HP2—nonactivated sample, HP3—30 min-activated sample with yttrium addition, and HP4—30 min-activated sample with graphene addition.

XRPD patterns of the sintered specimens are presented in Figure 2. Magnesium aluminate with the spinel structure is the only phase present in all samples and was identified using PDF card 01-077-1203. All peaks were well-defined, with high intensity, and are sharp, indicating high crystallinity. Rietveld analysis corroborated the presence of phasepure spinel in all sintered specimens, with crystallographic density of 3.584 g·cm^{-3}, which corresponds to its theoretical value. Lattice parameters were all about a = 8.077 Å. Neither mechanical activation nor additives affected lattice parameters significantly, indicating that neither carbon nor yttrium were likely substituted into the spinel lattice. Crystallite size determined by Rietveld refinement exhibited a maximum value of 429 Å for HP1, but decreased with the addition of yttrium or graphene with a minimum value of 391 Å for HP3. Incorporation of additives into spinel decreased both the lattice parameter and their crystallite size.
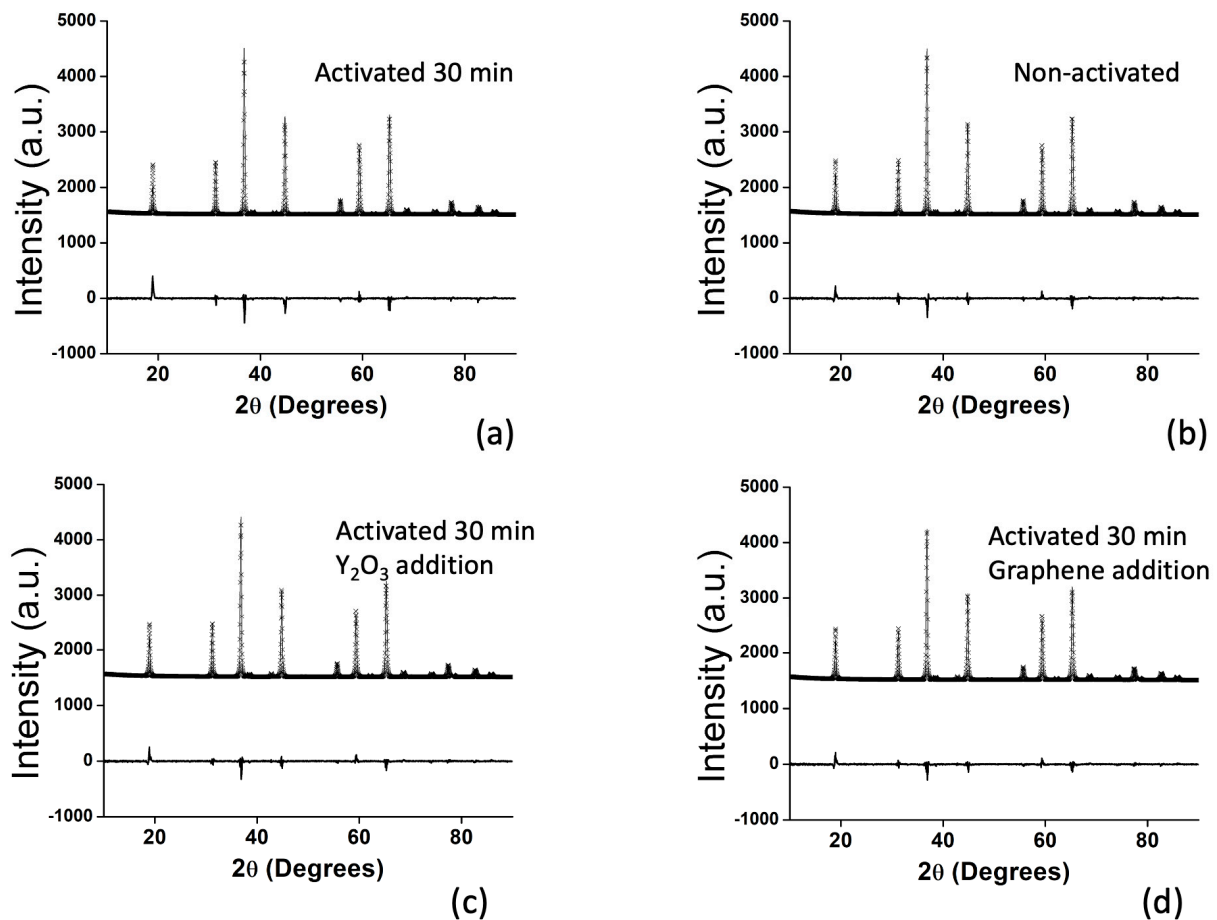
Figure 2. XRPD patterns and Rietveld fits of the sintered specimens: (**a**) HP1, (**b**) HP2, (**c**) HP3, and (**d**) HP4.

SEM images of sintered specimens are shown in Figure 3. All samples achieved a certain degree of translucency, indicating that the residual porosity was low [32]. Dense and homogeneous fully sintered matrix were characteristics of all samples. The nonactivated HP2 sample possesses the largest number of small, closed pores that were less than 200 nm, exhibiting a density of 3.46 g·cm^{-3} (96.5% TD). Voids larger than 1 μm were visible on the first three samples (HP1, HP2 and HP3), but were a consequence of grains being pulled out from the surface during the preparation process. A smaller number of closed spherical pores were visible on other micrographs (b, c, d), while the densest sample was the one with the yttrium addition (HP3), which reached more than 99.5% TD.

The spectral absorbance of samples is shown in Figure 4. The bands above ~11 μm wavelength were apparent in all samples, albeit with different depths. The relative differences between samples HP1-2-3 were due to compositional variations, such as the presence of Y_2O_3 and the contamination from milling media. The addition of graphene (sample HP4) increased the spinel spectral absorbance in the whole investigated wavelength range, and completely removed the complex spectral features shown by the other samples below 6 μm, bringing the curve to an almost flat, high-reflectance plateau. This major effect was obtained through both a reduction in the spectral reflectance in the range 0.3–6.0 μm (Figure 5a) and the zeroing of near-infrared spinel transparency window (see the transmittance curves in Figure 5b).
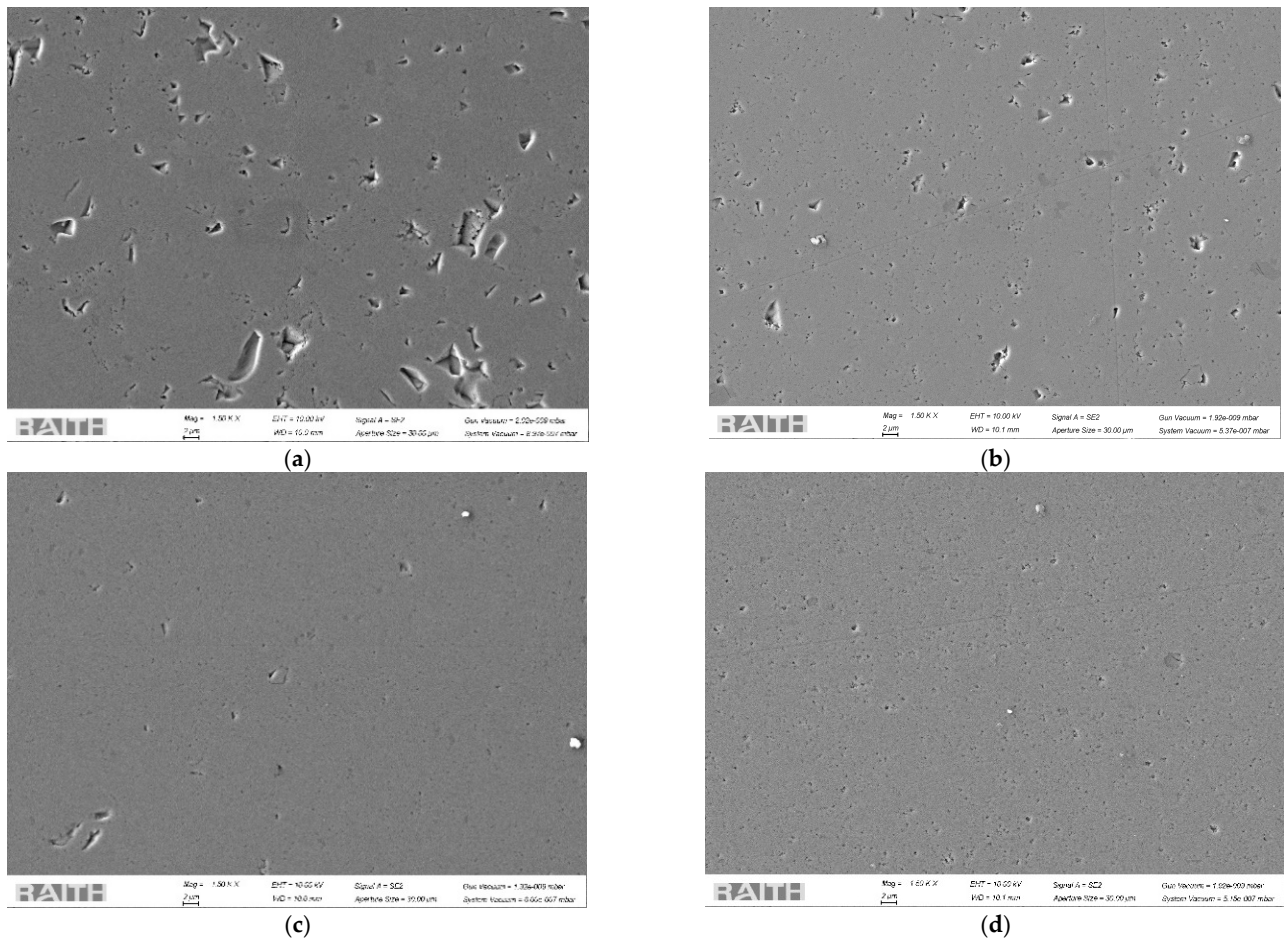
Figure 3. SEM images of sintered specimens: (**a**) HP1, (**b**) HP2, (**c**) HP3, and (**d**) HP4.

From the spectra, some parameters can be calculated to evaluate the potential of the materials as sunlight absorbers in solar receivers for thermodynamic solar plants. These parameters are solar absorptance α, total hemispherical emittance ε at the temperature T, and spectral selectivity α/ε, and are expressed by the following relationships:

$$\alpha = \frac{\int_{0.3\mu m}^{3\mu m} \alpha(\lambda) \cdot S(\lambda) d\lambda}{\int_{0.3\mu m}^{3\mu m} S(\lambda) d\lambda} \tag{2}$$

$$\varepsilon = \frac{\int_{0.3\mu m}^{15.7\mu m} \varepsilon(\lambda) \cdot B(\lambda, T) d\lambda}{\int_{0.3\mu m}^{15.7\mu m} B(\lambda, T) d\lambda} \tag{3}$$

where $S(\lambda)$ is the sunlight spectral distribution [33] and $B(\lambda,T)$ is the blackbody spectral radiance at the temperature T. For a more complete evaluation, the emittance in Equation (3) has been calculated at different temperatures from 800 to 1500 K. As a methodology comment referring to these parameters, the values calculated from Equations (1)–(3) were obtained from room-temperature spectra. These values are an estimation that is widely used in the literature for a comparative evaluation among materials. As such, they are not the exact values in operative conditions, which would need spectra acquired at the considered temperature. The methodology used herein generally underestimates the values of α and ε [34–36].
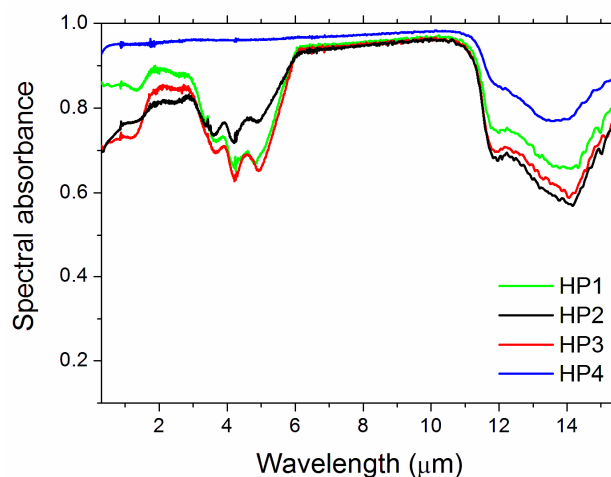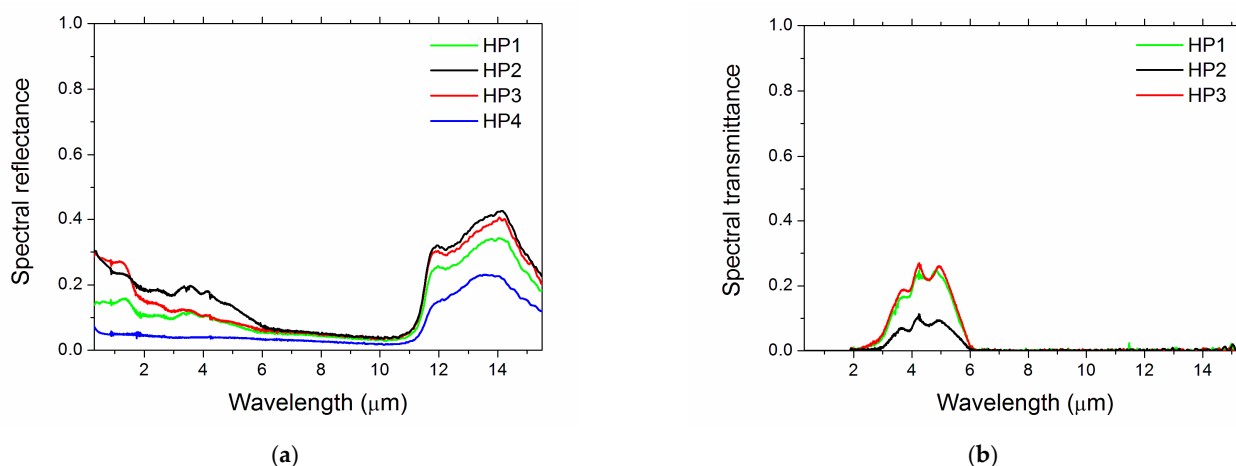
Figure 4. Room-temperature spectral absorbance.

(**a**)   (**b**)

Figure 5. Room-temperature spectral hemispherical reflectance (**a**) and spectral hemispherical transmittance (**b**). Sample HP4 shows a null transmittance in the whole investigated range, thus it does not appear in the plot.

The calculated α values are listed in Table 2. In addition, data for two reference samples of dense SiC were also added [37,38] because SiC is an advanced high-temperature solar receiver material that is currently employed in existing plants.

Table 2. Solar absorptance of sintered specimens, calculated from Equation (2) and of SiC pellets from [37,38].

| Sample	Solar Absorptance α
HP1	0.85
HP2	0.74
HP3	0.73
HP4	0.95
Dense SiC [37]	0.78
Dense SiC [38]	0.85

For an ideal solar absorber, α should be as close as possible to unity. From Table 2, the samples with the highest performance are HP4 and HP1, showing α values equal (HP1) or even better (HP4) than the best SiC. HP2 and HP3 can also be considered good solar absorbers, as their α values are comparable to those of the dense polished SiC [37].

When thermal emittance (Equation (3)) is considered, Figure 6 compares the spinel samples to the SiC pellets [39], showing that HP4 had black-body-like behaviour with high

thermal emittance, which is attributed to the graphene addition. The other spinel samples had emittance values similar to each other and comparable to SiC at temperatures above ~900 K. The spectral selectivity (α/ε ratio, Figure 7) shows that, at high temperatures, HP2 had a spectral selectivity similar to the more spectrally selective SiC specimens, while HP4 was similar to the second SiC reference pellet. Therefore, HP4 appears to be the most promising material from the present work for high-temperature solar thermal receivers, and should be comparable to SiC from the viewpoint of optical parameters.
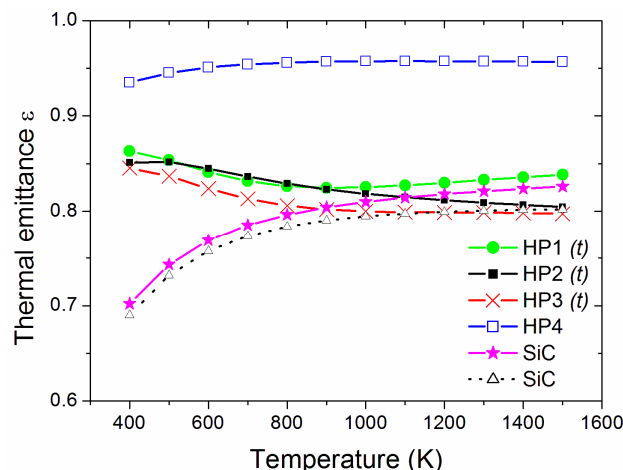
Figure 6. Estimated thermal emittance as a function of temperature. The label *(t)* identifies the samples showing transparency (non-null transmittance) at the considered thicknesses.
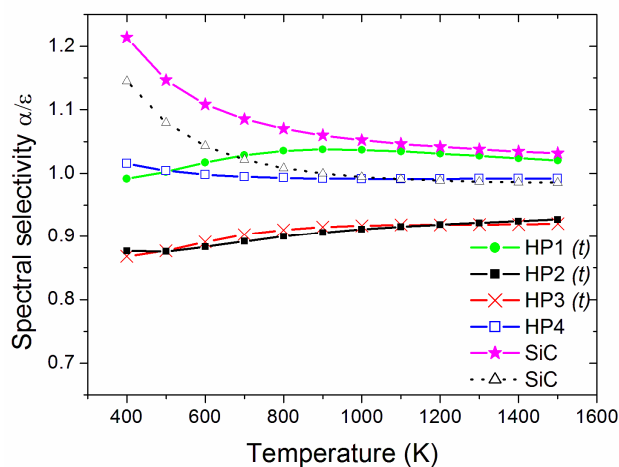
Figure 7. Estimated temperature-dependent spectral selectivity. The label *(t)* identifies the samples showing transparency (non-null transmittance) at the considered thicknesses.

Finally, given the spectral characteristics of the reflectance and transmittance spectra (Figure 5a,b) and considering that the range of nonzero transmittance is largely located in the infrared, outside the sunlight spectral region, increasing the transmittance by reducing the ceramic thickness could be beneficial in terms of optical parameters, as it reduces ε while only negligibly decreasing α, thus increasing the α/ε ratio. The optical performance of HP1, HP2 and HP3 samples could be improved using thinner specimens, combined, if needed for structural resistance, with a low-emittance substrate (e.g., a metal).

4. Conclusions

The influence of MA and additives was studied regarding the synthesis of $MgAl_2O_4$ spinel and its final properties. The focus was to monitor the influence of 30 min of mechanical activation along with additions of 0.1 wt.% Y_2O_3 and 1.0 wt.% graphene on

changes in the microstructure and optical properties. Both MA and additives are beneficial, and the main conclusions are:

- All specimens were nominally phase-pure spinel after HP. Dense, homogeneous and fully sintered microstructures were characteristic of all specimens. Nonactivated samples exhibited a larger number of closed spherical pores and lower relative densities (96.5% TD), while the densest sample was the one with Y_2O_3 addition (>99.5% TD).
- The samples with the highest optical performance were HP4 and HP1, showing α values equal to (HP1) or even better (HP4) than reported values for SiC. All samples could be good candidates for solar absorbers, but the sample with graphene addition appears to be the most promising sample for high-temperature solar thermal receivers. The optical parameters were comparable to SiC.

Author Contributions: Conceptualization, N.O. and W.G.F.; methodology, S.F. (Suzana Filipovic); software, C.C.; validation, D.S., S.F. (Simone Failla) and E.S.; formal analysis, B.A.M.; investigation, D.D.R.; resources, M.N.; data curation, N.O.; writing—original draft preparation, N.O.; writing—review and editing, B.A.M. and W.G.F.; visualization, N.O. and S.F. (Suzana Filipovic); supervision, W.G.F.; project administration, N.O.; funding acquisition, W.G.F. All authors have read and agreed to the published version of the manuscript.

Informed Consent Statement: Not applicable.

Conflicts of Interest: The authors declare no conflict of interest.

References

1. Zegadi, A.; Kolli, M.; Hamidouche, M.; Fantozzi, G. Transparent $MgAl_2O_4$ spinel fabricated by spark plasma sintering from commercial powders. *Ceram. Int.* **2018**, *44*, 18828–18835. [CrossRef]
2. Ianoş, R.; Lazău, I.; Păcurariu, C.; Barvinschi, P. Solution combustion synthesis of $MgAl_2O_4$ using fuel mixtures. *Mater. Res. Bull.* **2008**, *43*, 3408–3415. [CrossRef]
3. Esposito, L.; Piancastelli, A.; Martelli, S. Production and characterization of transparent $MgAl_2O_4$ prepared by hot pressing. *J. Eur. Ceram. Soc.* **2013**, *33*, 737–747. [CrossRef]
4. Obradović, N.; Filipović, S.; Đorđević, N.; Kosanović, D.; Marković, S.; Pavlović, V.; Olćan, D.; Đorđević, A.; Kachlik, M.; Maca, K. Effects of mechanical activation and two-step sintering on the structure and electrical properties of cordierite-based ceramics. *Ceram. Int.* **2016**, *42*, 13909–13918. [CrossRef]
5. Ting, J.; Lu, H.Y. Hot-pressing of magnesium aluminate spinel—II. Microstructure development. *Acta Mater.* **1999**, *47*, 831–840. [CrossRef]
6. Ting, J.; Lu, H.Y. Hot-pressing of magnesium aluminate spinel—I. Kinetics and densification mechanism. *Acta Mater.* **1999**, *47*, 817–830. [CrossRef]
7. Merac, M.R.; Reimanis, I.E.; Smith, C.; Kleebe, H.-J.; Müller, M.M. Effect of impurities and LiF additive in hot-pressed transparent magnesium aluminate spinel. *Int. J. Appl. Ceram. Technol.* **2013**, *10*, 33–48. [CrossRef]
8. Kim, J.M.; Kim, H.N.; Park, Y.J.; Ko, J.-W.; Lee, J.-W.; Kim, H.-D. Fabrication of transparent $MgAl_2O_4$ spinel through homogenous green compaction by micro fluidization and slip casting. *Ceram. Int.* **2015**, *41*, 13354–13360. [CrossRef]
9. Morita, K.; Kim, B.N.; Yoshida, H.; Hiraga, K.; Sakka, Y. Influence of spark plasma sintering (SPS) conditions on transmission of $MgAl_2O_4$ Spinel. *J. Am. Ceram. Soc.* **2015**, *98*, 378–385. [CrossRef]
10. Morita, K.; Kim, B.-N.; Yoshida, H.; Hiraga, K.; Sakka, Y. Assessment of carbon contamination in $MgAl_2O_4$ spinel during spark-plasma-sintering (SPS) processing. *J. Ceram. Soc. Jpn.* **2015**, *123*, 983–988. [CrossRef]
11. Sokol, M.; Kalabukhov, S.; Dariel, M.; Frage, N. High-pressure spark plasma sintering (SPS) of transparent polycrystalline magnesium aluminate spinel (PMAS). *J. Eur. Ceram. Soc.* **2014**, *34*, 4305–4310. [CrossRef]
12. Macaigne, R.; Marinel, S.; Goeuriot, D.; Saunier, S. Sintering paths and mechanisms of pure $MgAl_2O_4$ conventionally and microwave sintered. *Ceram. Int.* **2018**, *44*, 21107–21113. [CrossRef]
13. Obradović, N.; Fahrenholtz, W.; Filipović, S.; Kosanović, D.; Dapčević, A.; Đorđević, A.; Balać, I.; Pavlović, V. The effect of mechanical activation on synthesis and properties of $MgAl_2O_4$ ceramics. *Ceram. Int.* **2019**, *45*, 12015–12021. [CrossRef]

14. Reimanis, I.; Kleebe, H.J. A review on the sintering and microstructure development of transparent spinel ($MgAl_2O_4$). *J. Am. Ceram. Soc.* **2009**, *92*, 1472–1480. [CrossRef]

15. Sokol, M.; Halabi, M.; Kalabukhov, S.; Frage, N. Nano-structured $MgAl_2O_4$ spinel consolidated by high pressure spark plasma sintering (HPSPS). *J. Eur. Ceram. Soc.* **2017**, *37*, 755–762. [CrossRef]

16. Ye, G.; Troczynski, T. Mechanical activation of heterogeneous sol-gel precursors for synthesis of $MgAl_2O_4$ spinel. *J. Am. Ceram. Soc.* **2005**, *88*, 2970–2974. [CrossRef]

17. Dwibedi, D.; Avdeev, M.; Barpanda, P. Role of Fuel on Cation Disorder in Magnesium Aluminate ($MgAl_2O_4$) Spinel Prepared by Combustion Synthesis. *J. Am. Ceram. Soc.* **2015**, *98*, 2908–2913. [CrossRef]

18. Bratton, R.J. Co-precipitates yielding $MgAl_2O_4$ spinel powders. *Am. Ceram. Soc. Bull.* **1969**, *48*, 759–776.

19. Li, J.G.; Ikegami, T.; Lee, J.H.; Mori, T.; Yajima, Y. A wet-chemical process yielding reactive magnesium aluminate spinel ($MgAl_2O_4$) powder. *Ceram Int.* **2001**, *27*, 481–489. [CrossRef]

20. Filipović, S.; Pavlović, V.P.; Obradović, N.; Paunović, V.; Maca, K.; Pavlović, V.B. The impedance analysis of sintered $MgTiO_3$ ceramics. *J. of All. Comp.* **2017**, *701*, 107–115. [CrossRef]

21. Wang, S.; Zhang, J.; Luo, D.; Gu, F.; Tang, D.; Dong, Z.; Tan, G.; Que, W.; Zhang, T.; Li, S.; et al. Transparent ceramics: Processing, materials and applications. *Prog. Sol. St. Chem.* **2013**, *41*, 20–54. [CrossRef]

22. Wang, F.; Zhao, Y.; Yang, C.; Fan, N.; Zhu, J. Effect of MoO_3 on microstructure and mechanical properties of $(Ti,Mo)Al/Al_2O_3$ composites by in situ reactive hot pressing. *Ceram. Inter.* **2016**, *42*, 1–8. [CrossRef]

23. O'Quinn, E.C.; Shamblin, J.; Perlov, B.; Ewing, R.C.; Neuefeind, J.; Feygenson, M.; Gussev, I.; Lang, M. Inversion in $Mg_{1-x}Ni_xAl_2O_4$ Spinel: New Insight into Local Structure. *J. Am. Chem. Soc.* **2017**, *139*, 10395–10402. [CrossRef] [PubMed]

24. Torruella, P.; Ruiz-Caridad, A.; Walls, M.; Roca, A.G.; López-Ortega, A.; Blanco-Portals, J.; López-Conesa, L.; Nogués, J.; Peiró, F.; Estradé, S. Atomic-Scale Determination of Cation Inversion in Spinel-Based Oxide Nanoparticles. *Nano Lett.* **2018**, *18*, 5854–5861. [CrossRef] [PubMed]

25. Sickafus, K.E.; Wills, J.M.; Grimes, N.W. Structure of spinel. *J. Am. Ceram. Soc.* **1999**, *82*, 3279–3292. [CrossRef]

26. Abdi, M.S.; Ebadzadeh, T.; Ghaffari, A.; Feli, M. Synthesis of nano-sized spinel ($MgAl_2O_4$) from short mechanochemically activated chloride precursors and its sintering behavior. *Adv. Powd. Technol.* **2015**, *26*, 175–179. [CrossRef]

27. Obradović, N.; Fahrenholtz, W.G.; Filipović, S.; Corlett, C.; Đorđević, P.; Rogan, J.; Vulić, P.J.; Buljak, V.; Pavlović, V. Characterization of $MgAl_2O_4$ Sintered Ceramics. *Sci. Sinter.* **2019**, *51*, 363–376. [CrossRef]

28. Popova, N.A.; Lukin, E.S.; Pavlyukova, L.T.; Sevostyanov, M.A.; Leonov, A.V. Synthesis of alumomagnesian spinel by mechanical activation method. *IOP Conf. Ser. Mater. Sci. Eng.* **2019**, *525*. [CrossRef]

29. Tavangarian, F.; Li, G. Mechanical activation assisted synthesis of nanostructure $MgAl_2O_4$ from gibbsite and lansfordite. *Powd. Technol.* **2014**, *267*, 333–338. [CrossRef]

30. Peleš, A.; Đorđević, N.; Obradović, N.; Tadić, N.; Pavlović, V.B. Influence of prolonged sintering time on density and electrical properties of isothermally sintered cordierite-based ceramics. *Sci. Sinter.* **2013**, *45*, 157–164. [CrossRef]

31. Filipović, S.; Obradović, N.; Pavlović, V.B.; Mitrić, M.; Đorđević, A.; Kachlik, M.; Maca, K. Effect of consolidation parameters on structural, microstructural and electrical properties of magnesium titanate ceramics. *Ceram. Int.* **2016**, *42*, 9887–9898. [CrossRef]

32. Nečina, V.; Pabst, W. Grain growth of $MgAl_2O_4$ ceramics with LiF and NaF addition. *Open Ceram.* **2021**, *5*, 100078. [CrossRef]

33. ASTM G173-03. *Standard Tables for Reference Solar Spectral Irradiances: Direct Normal and Hemispherical on 37° Tilted Surface*; ASTM Int.: West Conshohocken, PA, USA, 2012.

34. Mercatelli, L.; Meucci, M.; Sani, E. Facility for assessing spectral normal emittance of solid materials at high temperature. *Appl. Optics.* **2015**, *54*, 8700–8705. [CrossRef] [PubMed]

35. Sani, E.; Mercatelli, L.; Meucci, M.; Zoli, L.; Sciti, D. Lanthanum hexaboride for solar energy applications. *Sci. Rep.* **2017**, *7*, 718. [CrossRef] [PubMed]

36. Azzali, N.; Meucci, M.; Di Rosa, D.; Mercatelli, L.; Silvestroni, L.; Sciti, D.; Sani, E. Spectral emittance of ceramics for high temperature solar receivers. *Sol. Energy* **2021**, accepted and in press. [CrossRef]

37. Sciti, D.; Silvestroni, L.; Mercatelli, L.; Sans, J.L.; Sani, E. Suitability of ultra-refractory diboride ceramics as absorbers for solar energy applications. *Sol. Energy Mater. Sol. Cells* **2013**, *109*, 8–16. [CrossRef]

38. Sciti, D.; Silvestroni, L.; Sans, J.L.; Mercatelli, L.; Meucci, M.; Sani, E. Tantalum diboride-based ceramics for bulk solar absorbers. *Sol. Energy Mater. Sol. Cells* **2014**, *130*, 208–216. [CrossRef]

39. Sani, E.; Sciti, D.; Capiani, C.; Silvestroni, L. Colored zirconia with high absorbance and solar selectivity. *Scr. Mater.* **2020**, *186*, 147–151. [CrossRef]